TESS asteroseismology of the Kepler red giants

Dennis Stello, Nicholas Saunders, Sam Grunblatt, Marc Hon, Claudia Reyes, Daniel Huber, Timothy Bedding, Yvonne Elsworth, Rafael García, Saskia Hekker, et al.

Monthly Notices of the ROYAL ASTRONOMICAL SOCIETY

MNRAS **512,** 1677–1686 (2022) https://doi.org/10.1093/mnras/stac414
Advance Access publication 2022 February 28

TESS asteroseismology of the Kepler red giants

Dennis Stello [1,2,3★] Nicholas Saunders,[4] Sam Grunblatt,[5,6] Marc Hon,[1,4] Claudia Reyes,[1] Daniel Huber,[4] Timothy R. Bedding [2,3] Yvonne Elsworth,[7] Rafael A. García,[8] Saskia Hekker [3,9,10] Thomas Kallinger,[11] Savita Mathur,[12,13] Benoit Mosser[14] and Marc H. Pinsonneault [15]

[1]*School of Physics, University of New South Wales, NSW 2052, Australia*
[2]*Sydney Institute for Astronomy (SIfA), School of Physics, University of Sydney, NSW 2006, Australia*
[3]*Stellar Astrophysics Centre, Department of Physics and Astronomy, Aarhus University, DK-8000 Aarhus C, Denmark*
[4]*Institute for Astronomy, University of Hawai'i, 2680 Woodlawn Drive, Honolulu, HI 96822, USA*
[5]*American Museum of Natural History, 200 Central Park West, Manhattan, NY 10024, USA*
[6]*Center for Computational Astrophysics, Flatiron Institute, 162 5thAvenue, Manhattan, NY 10010, USA*
[7]*School of Physics and Astronomy, University of Birmingham, Birmingham B15 2TT, UK*
[8]*AIM, CEA, CNRS, Université Paris-Saclay, Université Paris Diderot, Sorbonne Paris Cité, F-91191 Gif-sur-Yvette, France*
[9]*Center for Astronomy (ZAH/LSW), Heidelberg University, Königstuhl 12, D-69117 Heidelberg, Germany*
[10]*Heidelberg Institute for Theoretical Studies (HITS) gGmbH, Schloss-Wolfsbrunnenweg 35, 69118 Heidelberg, Germany*
[11]*Institute of Astrophysics, University of Vienna, 1180 Vienna, Austria*
[12]*Instituto de Astrofisica de Canarias, E-38200 La Laguna, Tenerife, Spain*
[13]*Departamento de Astrofisica, Universidad de La Laguna (ULL), E-38206 La Laguna, Tenerife, Spain*
[14]*LESIA, Observatoire de Paris, Université PSL, CNRS, SorbonneUniversité, Université de Paris, 92195 Meudon, France*
[15]*Department of Astronomy, The Ohio State University, Columbus, OH 43210, USA*

Accepted 2022 February 4. Received 2021 December 13; in original form 2021 April 27

ABSTRACT

Red giant asteroseismology can provide valuable information for studying the Galaxy as demonstrated by space missions like CoRoT and *Kepler*. However, previous observations have been limited to small data sets and fields of view. The TESS mission provides far larger samples and, for the first time, the opportunity to perform asteroseimic inference from full-frame images full-sky, instead of narrow fields and pre-selected targets. Here, we seek to detect oscillations in TESS data of the red giants in the *Kepler* field using the 4-yr *Kepler* results as a benchmark. Because we use 1–2 sectors of observation, our results are representative of the typical scenario from TESS data. We detect clear oscillations in ∼3000 stars with another ∼1000 borderline (low S/N) cases. In comparison, best-case predictions suggest ∼4500 detectable oscillating giants. Of the clear detections, we measure $\Delta\nu$ in 570 stars, meaning a ∼20 per cent $\Delta\nu$ yield (14 per cent for one sector and 26 per cent for two sectors). These yields imply that typical (1–2 sector) TESS data will result in significant detection biases. Hence, to boost the number of stars, one might need to use only $\nu_{\rm max}$ as the seismic input for stellar property estimation. However, we find little bias in the seismic measurements and typical scatter is about 5–6 per cent in $\nu_{\rm max}$ and 2–3 per cent in $\Delta\nu$. These values, coupled with typical uncertainties in parallax, $T_{\rm eff}$, and [Fe/H] in a grid-based approach, would provide internal uncertainties of 3 per cent in inferred stellar radius, 6 per cent in mass, and 20 per cent in age for low-luminosity giant stars. Finally, we find red giant seismology is not significantly affected by seismic signal confusion from blending for stars with $T_{\rm mag} \lesssim 12.5$.

Key words: stars: fundamental parameters – stars: interiors – stars: oscillations.

1 INTRODUCTION

The space-based asteroseismic revolution of red giant stars (de Ridder et al. 2009) spawned the realization that oscillating giants would provide powerful ways to study the Milky Way (Miglio et al. 2009). The initial attempts of this asteroseismically informed Galactic archaeology were made with CoRoT (e.g. Miglio et al. 2013; Anders et al. 2017) and later with *Kepler* (e.g. Casagrande et al. 2016; Sharma et al. 2016; Silva Aguirre et al. 2018). However, it soon became clear that the small sky coverage and the complex, and to some degree undocumented, target selection function would limit the use of these particular data sets within this line of research. Fortunately, *Kepler's* K2 mission (Howell et al. 2014) gave birth to the K2 Galactic Archaeology Programme, designed to support studies of the Milky Way along the ecliptic, with stars probing many different parts of the Galaxy and following a simple reproducible selection function (Stello et al. 2015; Sharma et al. 2021a). Although seismic data have been released for all campaigns of the K2 Galactic Archaeology Programme (Stello et al. 2017; Zinn et al. 2020, 2022), the scientific fruits of this rich data set have only just started to be harvested (Khan et al. 2019; Rendle et al. 2019; Sharma et al. 2019, 2021b)

The launch of NASA's TESS mission opened the first opportunity to detect oscillations in red giants over the full sky (Ricker et al. 2015; Campante et al. 2016), with its initial 2-yr mission covering

★ E-mail: stello@physics.usyd.edu.au

first the Southern ecliptic hemisphere, followed by the Northern hemisphere. The potential to study large stellar populations in the Milky Way with TESS is therefore significant. In an early attempt to quantify the asteroseismic performance of TESS in this context, Aguirre et al. (2020) used TASOC[1] 'FastTrack' data of 25 bright red giants ($V \simeq 6$) from the first two sectors of TESS's Southern hemisphere observations. They found all the giants in their sample showed oscillations, confirming the expected TESS performance. When combining the seismology from TESS with parallaxes from Gaia DR2 (Gaia Collaboration et al. 2018), they found the precision on the inferred stellar radii, masses, and ages from grid modelling was similar to that obtained from 4-yr *Kepler* data. This showed that the smaller aperture and shorter observation time span by TESS (leading to less precise seismic measurements) is compensated in the grid modelling by the targets being brighter and closer (more photons and more precise parallaxes) compared to the typical *Kepler* targets. Later, Mackereth et al. (2021) used a full-year (13 sectors) of TESS Southern-continuous-viewing-zone data, covering about 450 deg^2, to infer the potential for red giant asteroseismology with TESS across its full-sky view. They estimated ~300 000 giants would show oscillations across the sky.

During its second year, TESS covered the *Kepler* field in Sectors 14 (fully) and 15 (partly). This provided an interesting opportunity to test the TESS performance in more detail on a large sample of well-studied red giants. Despite the limitations of the *Kepler* data for Galactic archaeology studies, the mission provides the best-quality data for red giant seismology on individual stars. As such, *Kepler* is still the benchmark for red giant seismology. The nearly continuous observations for four years, stable environment far from the Earth, and relatively large aperture mean that *Kepler*-based results will probably remain the ultimate 'ground truth' for the foreseeable future. In addition to testing the TESS performance, the TESS observations of the *Kepler* red giants also give us an important way to verify whether our seismic measurements are consistent with the 'true' values, as we move toward analysing all TESS data fully automatically in the future.

In this paper, we use the *Kepler* results on red giants to study how well we can measure the oscillations from TESS data of all giants in the *Kepler* field brighter than Kp = 13. Particularly, we want to (1) investigate how the intrinsic limitations of TESS (such as small aperture and short observation time) affect the completeness of the seismic stellar population from TESS, (2) study if the uncertainties on the seismic observables $\nu_{\rm max}$ and $\Delta\nu$ are representative of the true uncertainties, (3) estimate the yield of stars with reliable $\Delta\nu$ measurements as opposed to only $\nu_{\rm max}$, (4) see if there is any bias in $\nu_{\rm max}$ and $\Delta\nu$ relative to the *Kepler* results, and finally, (5) provide a rough estimate of the radius, mass, and age precision one can expect from the one to two sectors of TESS observations.

2 TARGET SELECTION AND LIGHT CURVE CREATION

We selected the 8668 stars brighter than Kp=13 in the catalogue of 16 000 *Kepler* red giants with detected oscillations by Yu et al. (2018). These stars were all observed with *Kepler's* 30-min cadence and have a measurement of the frequency of maximum acoustic power, $\nu_{\rm max}$, and of the frequency separation between radial overtone modes, $\Delta\nu$.

To cover as many stars as possible, we used the TESS Full Frame Images taken at 30-min cadence as our data source. We followed the approach of Saunders et al. (2022)[2], which we summarise here. First, we retrieved data from the Mikulski Archive for Space Telescopes (MAST) using `TESScut` (Brasseur et al. 2019) to download 11 x 11-pixel cutouts around each target, and then applied the following methodology to remove the scattered light background from the TESS Full Frame Image observations. Our pipeline uses the `RegressionCorrector` framework in the `lightkurve` Python package (Lightkurve Collaboration et al. 2018). Using the cutout target pixel files, we created a design matrix with column vectors populated by the flux light curves of pixels outside a threshold aperture mask, avoiding pixels that contain flux from the target to ensure our noise model did not fit out the desired signal. We then performed Principal Component Analysis on the columns of the design matrix to find ten principal components to use in our model. To produce our final noise model, we set up a generalized least-squares problem to find optimal coefficients for each of the components in our design matrix, and then generated a model as a linear combination of the column vectors. We produced an uncorrected light curve by performing simple aperture photometry on the cutout target pixel file using the inverse of the aperture mask used to select regressors. Our final light curves were produced by subtracting the noise model from the uncorrected light curves.

Almost all the selected stars were observed in Sector 14 (8576 stars) and about half were observed in Sector 15 (4909 stars). We concatenated the light curves of those observed in both sectors (4817 stars). We then followed the data processing previously applied to K2 data by Stello et al. (2015) and Stello et al. (2017), which included a 4-d wide boxcar high-pass filter (meaning a cut-off frequency of about 3 μHz in the frequency domain) and filling gaps below 1.5 h in length using linear interpolation.

For each sector, we identified the time stamp segments (spacecraft orbital phases) for which the light curves were potentially affected by Earth shine and subsequently removed affected stars.[3] Affected stars were defined as those with a light curve standard deviation in their potential Earth shine segments, $\sigma_{\rm Earth}$, above 40 per cent of their unaffected segments, $\sigma_{\rm normal}$. We removed 2307 stars in this process.

Fig. 1(a) shows the sky coverage of our targets for Sector 14, revealing the footprint of the *Kepler* field of view. The colour-code of each observed star represent $\sigma_{\rm Earth}/\sigma_{\rm normal}$. The part of the field affected by Earth shine (bright coloured dots) corresponds to TESS camera 1. The two insets show example light curves with the segments potentially affected by Earth shine highlighted in red. In Sector 15, the Earth shine issue is clearly less severe, only affecting the lower-right corner of the field, as seen in Fig. 1(b). The inset in this figure shows the $\sigma_{\rm Earth}/\sigma_{\rm normal}$ distribution and the cut-off (dashed line) used to remove affected stars.

We also found and removed an additional 196 stars that showed orders-of-magnitude higher noise than the rest of the sample, with a standard deviation $\sigma_{\rm normal} > 0.005$. All turned out to lie close to the TESS CCD edges (Figs 1c–d). For the remaining 6165 stars, we calculated the Fourier transform (power spectrum) for subsequent oscillation analysis. In Fig. 2 (left-hand panels), we show a representative set of the power spectra from TESS. In the right-hand panels, we illustrate the corresponding *Kepler* data, which can be regarded as providing the ground truth benchmark measurements in this investigation. We note that amplitude calibration between TESS and *Kepler* is still uncertain [Lund et al. (in preparation)] but

[1]TESS Asteroseismic Science Operations Center: http://www.tasoc.dk

[2]https://github.com/nksaunders/giants

[3]Although one could potentially salvage affected stars by removing only the affected time segments, we opted not to do so for our purpose.

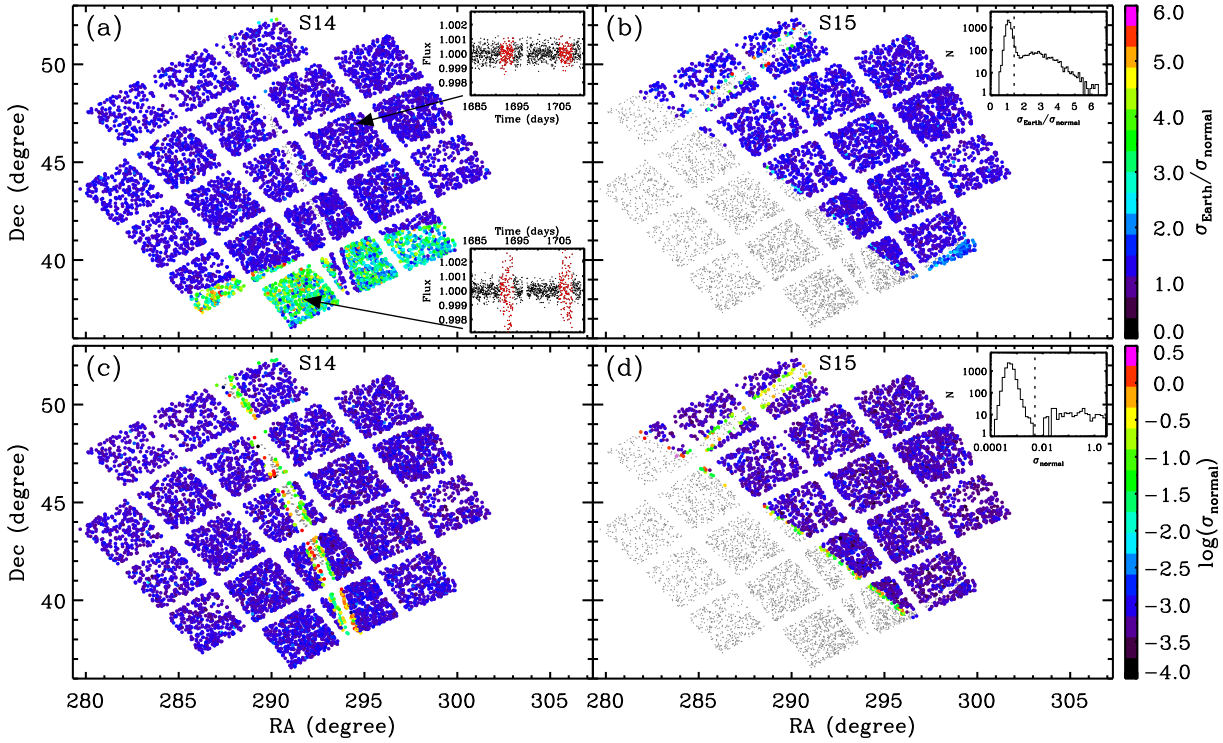

Figure 1. Sky coverage of our targets (grey points). Panel (a) Observed stars in TESS Sector 14 are colour-coded by $\sigma_{\rm Earth}/\sigma_{\rm normal}$. The insets show two example light curves, with the time stamps used to calculate the scatter colour-coded by red ($\sigma_{\rm Earth}$) and black ($\sigma_{\rm normal}$) points. Panel (b) Same as panel (a) but for Sector 15. The inset shows the $\sigma_{\rm Earth}/\sigma_{\rm normal}$ distribution and the cut-off value of 1.4. Panel (c) Same as panel (a) but colour-coding showing $\log(\sigma_{\rm normal})$. Panel (d) Same as panel (c) but for Sector 15. The inset shows the $\sigma_{\rm normal}$ distribution and the cut-off value of 0.005.

will not affect the results presented here. Thirty stars in our sample also had 2-min cadence TESS data, and hence an existing SPOC light curve on MAST, and comparison of those power spectra with ours showed on average similar power levels across all frequencies, although with some star-to-star variation.

3 DETECTION OF OSCILLATIONS

For Galactic archaeology, in particular, we would like our seismic detection algorithms to provide complete and pure samples, meaning we detect all possible detections without introducing any false positives. Stello et al. (2017) demonstrated that visual inspection of power spectra provided a robust determination of which stars showed oscillations (high completeness and high purity), despite being subjective and time consuming. Based on this, and previous work by Hekker et al. (2011) and Hekker et al. (2012), Yu et al. (2018) used visual inspection to classify detections and non-detections for their sample of 16 000 *Kepler* red giants, now regarded as a gold standard data set from the *Kepler* red giants (e.g. Mackereth et al. 2021). To eliminate the shortcomings of performing visual inspection manually, Hon, Stello & Zinn (2018b) trained an image-recognition artificial neural network on such visual classification, which was shown to be very efficient on *Kepler* data (Hon et al. 2019). However, this network has not yet been trained to provide both pure and complete sets of detections from actual TESS data. We therefore followed the approach by Stello et al. (2017) to manually classify our relatively small sample of TESS stars into three detection categories: 'Yes', 'Maybe', and 'No'. These results helped inform our subsequent results when we came to assess how well we could measure the seismic, as well as fundamental global, properties of the stars.

Fig. 3 shows the entire sample of stars, with the detection of oscillations by TESS indicated by colour. We see that the detections (Fig. 3a, green) follow a similar threshold trend in the upper right corner to that predicted using the formalism in Chaplin et al. (2011) and Schofield et al. (2019) (black line). For the predictions, we ignored blending and systematic noise and different to the approach by Schofield et al. (2019), we used *Gaia*-based radii directly from the TESS Input Catalog (Stassun et al. 2019) and used TESS magnitudes in place of Johnson I-band. Fainter and intrinsically less luminous stars (lower amplitude and larger $\nu_{\rm max}$) have a signal-to-noise ratio too low to detect the oscillations. Extrapolating the threshold line towards the most luminous giants with $\nu_{\rm max} \sim 5$–$10\,\mu$Hz, suggests that TESS would probably be able to detect oscillations in stars as faint as $T_{\rm mag} \sim 14$, at least for the most luminous stars. As expected, most of the 'Maybe' detections (Fig. 3b magenta) are close to the detection threshold; they truly are borderline cases. Many of them are situated in the red clump (RC) region around $\nu_{\rm max} \sim 30$–$100\,\mu$Hz, which often provide lower and wider oscillation power excess detections (e.g. Mosser et al. 2012; Yu et al. 2018). While most non-detections (Fig. 3c, red) are above the predicted threshold line, as expected, many fall well within the predicted 'detection' region below the line. Based on spot checks, many of them show either unusually strong low-frequency variation (regular or irregular, indicative of binarity or instrumental/photometric issues) or significantly different noise levels between the two observing sectors. This strong overlap between detections and non-detections in $\nu_{\rm max}$–$T_{\rm mag}$ space is only seen in the observations. The detection predictions show very little overlap if plotted in the $\nu_{\rm max}$–$T_{\rm mag}$ diagram. This is a result of ignoring any systematics, demonstrating that the predictions represent the ideal scenario (single well-isolated stars and a perfectly

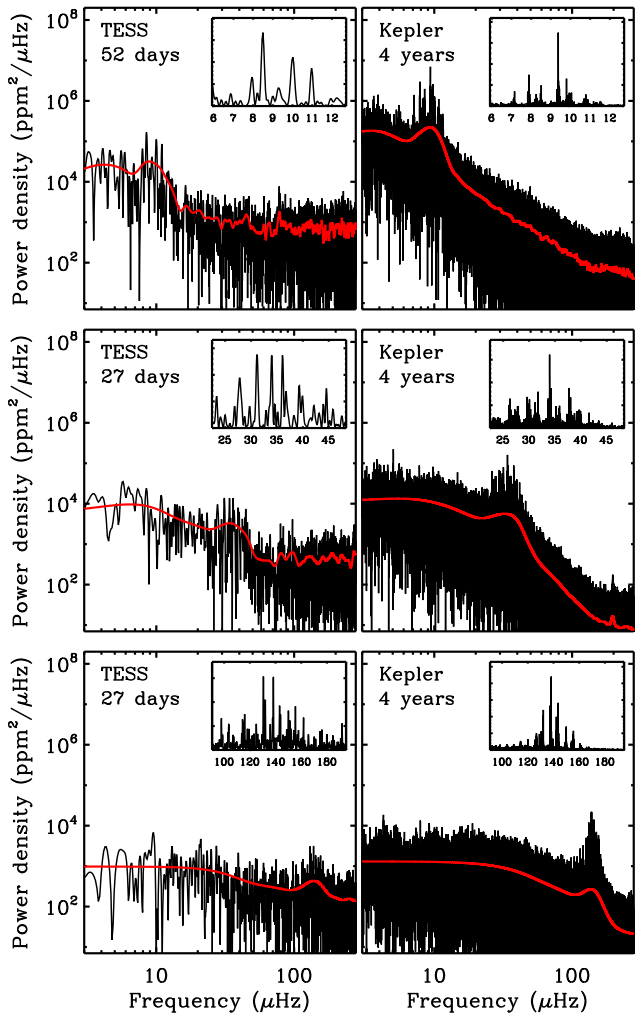

Figure 2. Example power spectra from TESS (left-hand panels) and *Kepler* (right-hand panels) for three stars ranging from low to high $\nu_{\rm max}$ values. The red curves show the smoothed spectra using the same smoothing for TESS and *Kepler*.

performing instrument and photometric extraction). With this in mind, we count the number of stars with a predicted detection probability larger than 99 per cent to be about 4500. Hence, the observed yield relative to this optimistic scenario is ∼60 per cent for clear detections (2724 stars), and ∼80 per cent if the stars marked 'Maybe' are also counted as genuine detections (975 stars). We note that these yields are not like-for-like comparable to those of Mackereth et al. (2021) because our studies are complementary. Differences between the two studies include: (1) the length and filtering of the time series, (2) the target selection, and (3) the definitions for what constitutes a detection.

To further verify whether our detections follow expectations, Fig. 4 shows the average power in the TESS data as a function of *Kepler* $\nu_{\rm max}$, measured in a $0.4\nu_{\rm max}$-wide window around the *Kepler* $\nu_{\rm max}$. The clear detections (Fig. 4a) show a relatively tight power-law relation with a sharp upper limit at fixed $\nu_{\rm max}$, as seen in previous ensemble results (e.g. Yu et al. 2018), demonstrating that the power spectrum is dominated by oscillation power at $\nu_{\rm max}$. This is further supported by the power measured for a given star typically being much larger than the predicted white noise for its brightness (dots fall above dashed lines of the same colour). Most of the 'Maybe' detections (Fig. 4b) also seem to follow the power-law relation and power levels being higher than the predicted white noise, suggesting that they are mostly genuine detections. The non-detections, however, mostly follow a flat and quite broad distribution (at fixed $\nu_{\rm max}$), with many stars falling near and even below the predicted noise, which shows the power spectra are dominated by noise. It is evident, however, that towards low $\nu_{\rm max}$, some non-detections start to follow the steep power law of the detections, suggesting that some of these stars could possibly show hints of oscillation power.

4 SEISMIC MEASUREMENTS

In the next step, we analysed the level of precision and accuracy in $\nu_{\rm max}$ and $\Delta\nu$ from the TESS data by benchmarking our results against the 4 yr-based *Kepler* results by Yu et al. (2018). The assumption is that the *Kepler* results can be regarded as the ground truth, with negligible uncertainty relative to those of the TESS measurements. To make a like-for-like comparison, we followed the approach by Yu et al. (2018) to extract $\nu_{\rm max}$ and $\Delta\nu$ using the so-called SYD pipeline by Huber et al. (2009), with improvements detailed in Huber et al. (2011) and Yu et al. (2018). Here, we only looked at stars deemed clear detections in the previous section.

The direct comparison between the TESS and *Kepler* results is shown in Fig. 5(a) for $\nu_{\rm max}$ and Fig. 5(b) for $\Delta\nu$. The deviations from the dashed 1-to-1 line are completely dominated by the uncertainty in the TESS measurements (see representative 3σ error bars for TESS; *Kepler* error bars are too small to see). The tight correlation in Fig. 5(a) confirms that our detections with TESS are robust. A similar plot of the 'Maybe' cases also reveals a tight relation, further supporting that most are genuine detections, while the 'No' detections show an extremely large scatter indicative of random numbers. Almost all the outliers seen in Fig. 5(b) have reported TESS uncertainties above 10 per cent.

It is evident from Fig. 5(a) that 1–2 sectors of TESS data will provide relatively few seismic detections of low-luminosity red giant branch stars ($\nu_{\rm max} \gtrsim 100$ μHz) and of highly luminous giants ($\nu_{\rm max} \lesssim 5$ μHz), with the bulk of detections being in the helium-core burning RC stars ($\nu_{\rm max} \sim 30$–40 μHz) (see also Fig. 3). Unfortunately, RC stars are typically the most difficult when it comes to extracting $\Delta\nu$ reliably from short time series, as evident from the larger spread in the RC region of Fig. 5(b) ($\Delta\nu \sim 3$–4 μHz).

We know from previous careful visual inspection of K2 results, which covered ∼ 80 d, that only about 50 per cent of the stars with oscillation power excess (a $\nu_{\rm max}$ detection) also provided reliable $\Delta\nu$ measurements (Stello et al. 2017). With one or two sectors of TESS data (27 or 54 d), we would therefore expect somewhat lower yields. To verify which stars had reliable $\Delta\nu$ detections, we used an improved version of the artificial neural network by Zinn et al. (2020), trained on one- and two-sector-long K2 data sets (Reyes et al. 2022). We found that 570 stars showed reliable $\Delta\nu$ detections; hence an overall yield of 20 per cent. In Table 1, we quantify the $\Delta\nu$ yields for different samples of stars and show how it depends on having one or two sectors of data. In addition to the shorter observations by TESS compared to K2, one reason why these yields are lower than for K2 could be that the lower signal-to-noise ratio in the TESS data (compared to K2), excludes predominantly low-luminosity red giant branch stars, which would typically provide a high fraction of $\Delta\nu$ detections due to their well-resolved simple frequency patterns (Bedding et al. 2010).

In Fig. 6, we show the overall fraction of stars with $\Delta\nu$ measurements within 3 per cent and 1 per cent of the *Kepler* values as

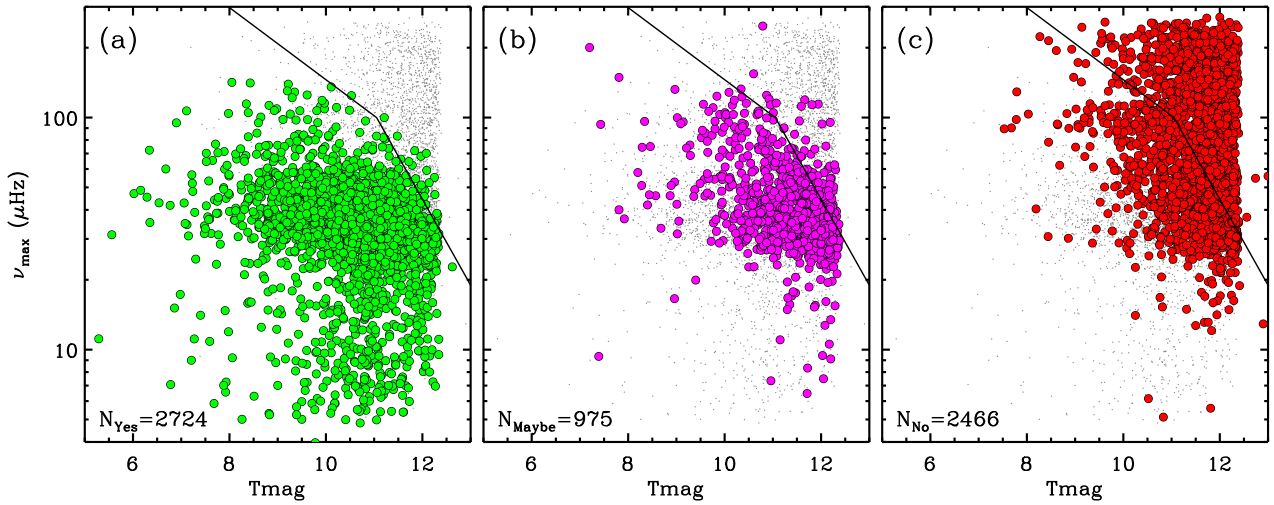

Figure 3. *Kepler* values of ν_{max} from Yu et al. (2018) versus TESS magnitude from Stassun et al. (2019) of all stars seismically analysed here (grey dots). In each panel, they are colour-coded according to our detection of oscillations in TESS data: (a): Yes (green), (b): Maybe (magenta), and (c): No (red). The black line shows the predicted detection threshold for TESS.

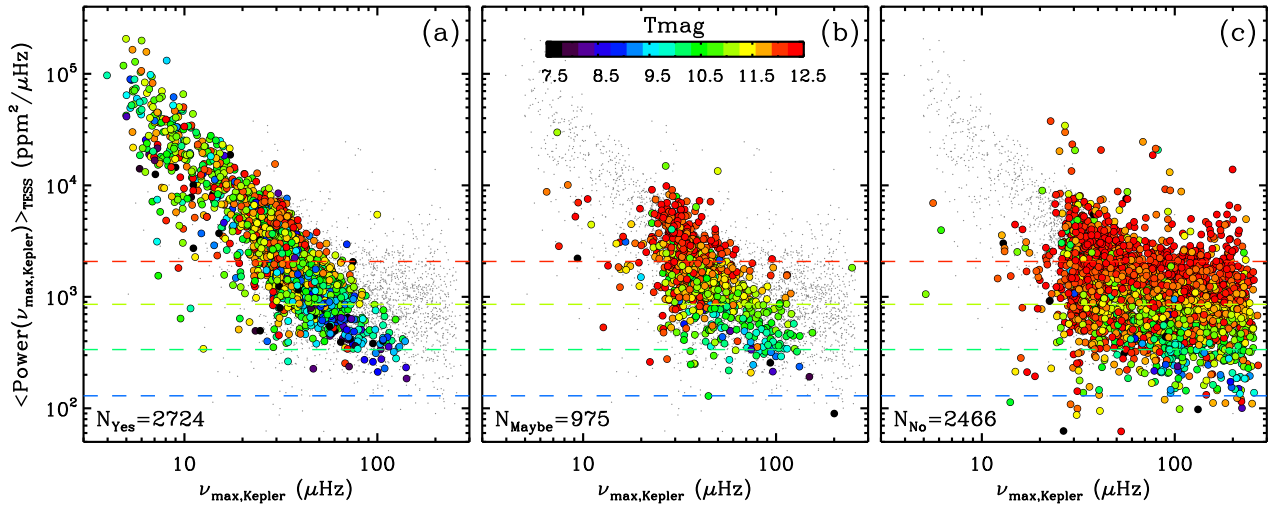

Figure 4. Average power in the TESS data around ν_{max} from Yu et al. (2018) versus ν_{max} of all the seismically analysed stars (grey dots). The colour-highlighted stars are separated into three panels according to their detection classification like in Fig. 3 [(a) : Yes; (b): Maybe; (c): No], but with the colour-coding showing T_{mag}. The dashed lines show the white noise levels according to equation (11) in Campante et al. (2016) for T_{mag} = 9, 10, 11, and 12.

a function of ν_{max} to further demonstrate where the most and best results are expected. In combination, Table 1, Figs 3, 5, and 6 imply that all regions of the parameter space (be it seismic or in brightness), and hence the stellar evolutionary stage, are affected by detection bias. This clearly needs to be taken into account when assessing the completeness of the seismic samples for the purpose of population studies.

We now turn to the measurement uncertainties. The red histogram in Fig. 7(a) shows the fractional deviation of the TESS ν_{max} from the *Kepler* result ($|\nu_{max\,TESS} - \nu_{max\,Kepler}|/\nu_{max\,Kepler}$). This deviation from the 'true' value allows us to check if the reported uncertainties from the SYD pipeline are robust across the ensemble as a whole; in other words, whether they are representative of the true measurement uncertainties. The blue curve in Fig. 7(a) shows the deviation one would expect from the reported uncertainties. We derived each deviation by taking a random extract from a Gaussian distribution with a width $2\sqrt{2\ln 2}$ times the reported uncertainty for each star.[4] The distributions have similar shapes, although it seems the reported ν_{max} uncertainties are on average underestimated by about 10–30 per cent.

Fig. 7(b) shows the plot similar to Fig. 7(a), but for $\Delta\nu$. The reported uncertainties are clearly accurate, with typical values of about 2–3 per cent, similar to what was reported by Aguirre et al. (2020) on about a dozen bright stars. This shows their results on radius, mass, and age precision are representative for the full sample of red giants observed during 1–2 sectors by TESS when using grid-based modelling, including parallax information, as performed by

[4]Adding the measurement uncertainty from the *Kepler* result to the width of the Gaussian did not significantly change the final distribution, as shown in the figure.

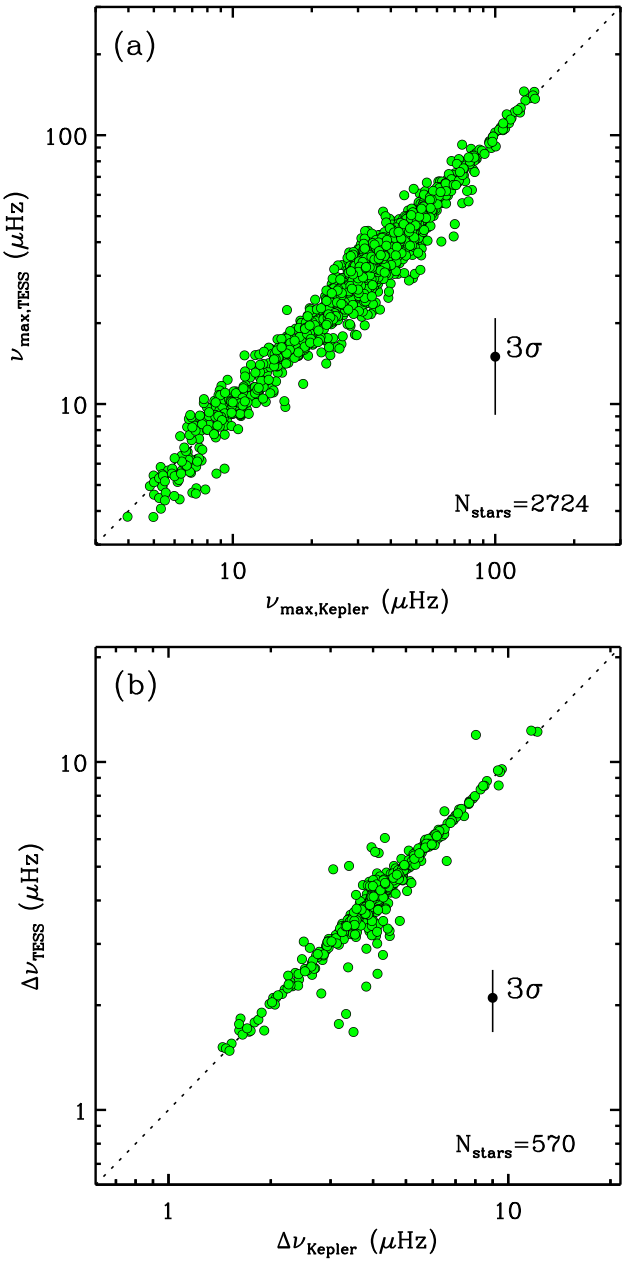

Figure 5. TESS versus *Kepler* results for both ν_{max} [panel (a)] and $\Delta\nu$ [panel (b)]. Only stars with confirmed oscillations are shown in panel (a), while panel (b) shows only the subset that also have $\Delta\nu$ deemed reliable using our neural network vetter (Reyes et al. 2022). The outliers have large quoted uncertainties. The 3σ error bar represents the median uncertainties of the TESS data (the error bars for *Kepler* are too small to be visible).

Table 1. $\Delta\nu$ yields.

Sample	1 sector (per cent)	2 sectors (per cent)
Full	14	26
RGB/AGB	20	48
RC*	12	19

Note. *Red clump (RC) star identifications are from Hon, Stello & Yu (2018a).

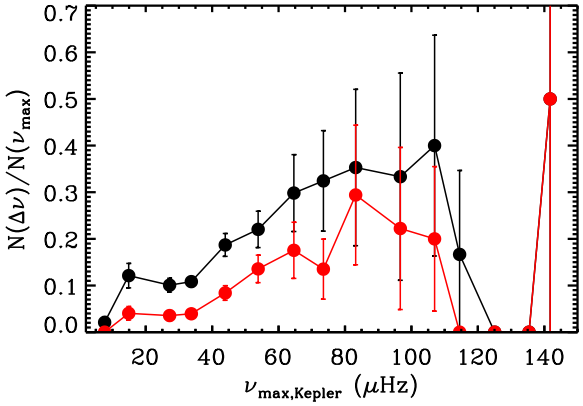

Figure 6. Fraction of stars with a $\Delta\nu$ measurement to better than 3 per cent (black curve) and 1 per cent (red curve).

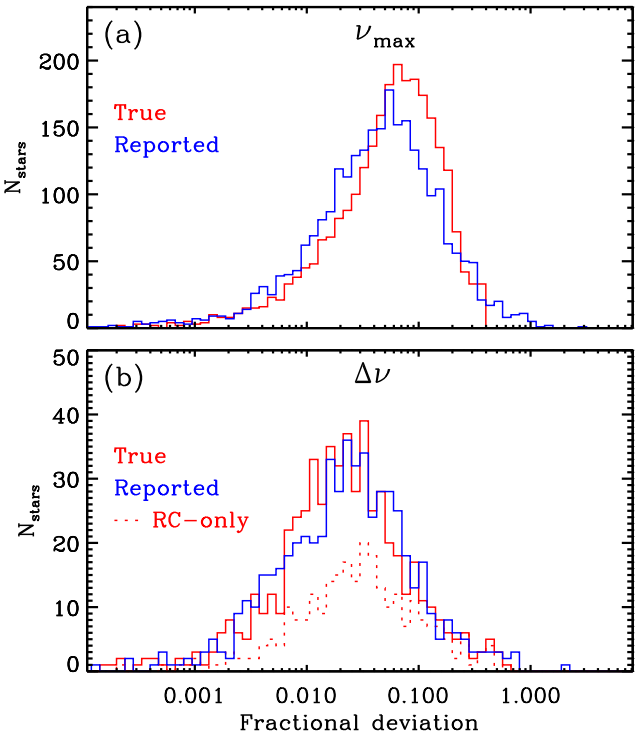

Figure 7. Deviations of TESS results for both ν_{max} and $\Delta\nu$ are shown in panels (a) and (b), respectively. 'True' deviations are |'TESS'−'*Kepler*'|/'*Kepler*'. 'Reported' deviations are random extracts from N(0,$\sigma_{'TESS'}$/'TESS') distributions.

Aguirre et al. (2020). The figure also illustrates that the RC stars typically have larger uncertainties (red dashed line) than red giant branch stars, as expected from their more complicated frequency patterns in the power spectra.

In addition to random errors, we also want to investigate potential systematics between TESS and *Kepler* results because it can affect comparisons of inferred masses and hence ages of the stars between the two data sets. Any bias could be either from difference in the data or because the time series are not the same length, which could affect the automated fitting procedures in the data analysis. In Fig. 8, we show the fractional difference between TESS and *Kepler* as a function of ν_{max} and $\Delta\nu$. Overall there is no strong bias (-0.004 ± 0.003 for ν_{max} and 0.004 ± 0.002 for $\Delta\nu$). However, for the RC stars with ν_{max}

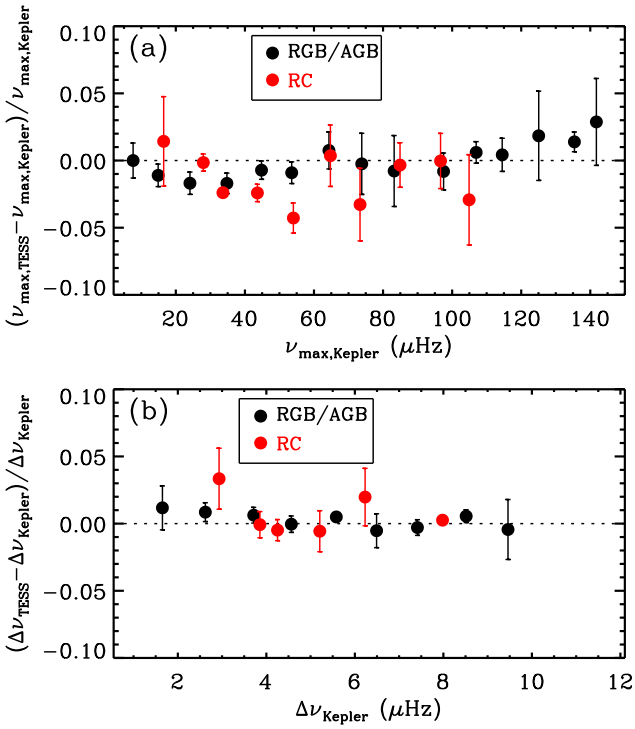

Figure 8. Binned fractional difference between TESS and *Kepler* for both ν_{max} and $\Delta\nu$ is shown in panels (a) and (b), respectively. RC star identifications are from Hon et al. (2018a).

around 40 μHz, the TESS ν_{max} results tend to be 2–3 per cent lower than for *Kepler*. For red giant branch stars at high ν_{max}, there is also evidence of some bias (TESS values being larger), but the few data points in these bins make this somewhat more uncertain.

Finally, we wanted to quantify the scatter in results across the different seismic analysis pipelines that are typically used in large ensembles efforts (Pinsonneault et al. 2014, 2018). This would act as a way to estimate pipeline-dependent systematic uncertainties in the seismic analysis of TESS data. The pipelines were only given the 2724 stars that had confirmed oscillations, and were only asked to provide results deemed reliable. The pipelines engaged in this analysis were the so-called, A2Z (Mathur et al. 2010; García et al. 2014), BAM (Zinn et al. 2019), BHM (Elsworth et al. 2017), CAN (Kallinger et al. 2010b), COR (Mosser & Appourchaux 2009), and OCT (Hekker et al. 2010) updated with packages from TACO [Hekker et al. (in preparation)]. We derived the scatter across pipelines for each star for which at least four pipelines reported a measurement (∼2500 stars). The ν_{max} scatter distribution peaked at 2 per cent, with a slight ν_{max}-dependent trend. At (low) $\nu_{max} = 10$–20 μHz the scatter was around 3 per cent, while at (high) $\nu_{max} = 90$–100 μHz the scatter was around 0.5 per cent. We found 8 per cent of the stars had at least one pipeline return an outlier measurement. For $\Delta\nu$, the scatter distribution also peaked at 2 per cent and with a slight ν_{max}-dependent trend. At (low) $\nu_{max} = 10$–20 μHz the scatter was around 2–3 per cent, while at (high) $\nu_{max} = 90$–100 μHz the scatter was around 1–2 per cent. About 24 per cent of the stars had at least one pipeline return an outlier measurement.[5] These scatter values indicate that the pipeline-dependent systematics are typically smaller than the uncertainties on the individual seismic measurements that are shown in Fig. 7.

[5]For additional recent details into the biases between pipelines on short time series see for example Stello et al. (2017) and Zinn et al. (2022).

5 UNCERTAINTY ON RADIUS, MASS, AND AGE

Now we turn to the measurement uncertainties on the fundamental stellar properties, which ultimately determine how useful the 1–2 sector red giant data will be for studying the Milky Way. Based on our results, we expect the minority of the TESS seismic red giant sample will have both ν_{max} and $\Delta\nu$ measurements available. We therefore consider two scenarios separately; one where both ν_{max} and $\Delta\nu$ are available and one where we only have ν_{max}.

We are now in the *Gaia* era, which gives us powerful additional tools for asteroseismology. Scaling relations are distance-independent, but also highly sensitive to uncertainties in the measurements. The ν_{max} and $\Delta\nu$ scaling relations give us $R \simeq T_{eff}^{0.5}\nu_{max}/\Delta\nu^2$ and $M \simeq T_{eff}^{1.5}\nu_{max}^3/\Delta\nu^4$ (Brown et al. 1991; Kjeldsen & Bedding 1995; Kallinger et al. 2010a); all variables in terms of solar values, which we assumed to have negligible uncertainty. The utility of a fully asteroseismic approach thus degrades dramatically with increased errors. However, with an independent radius estimate, it is possible to infer masses using either ν_{max} or $\Delta\nu$ alone. *Gaia* data can be used to infer luminosity, from a combination of photometry, astrometry, and extinction maps. When combined with spectroscopy, this yields what we will refer to as a *Gaia* radius. It is easier to measure ν_{max} in TESS data, so following Stello et al. (2008), we focus here on ν_{max} plus R as an alternative scaling relation. In this case, $M \simeq T_{eff}^{0.5}\nu_{max}R_{Gaia}^2$. For a sufficiently precise R, the uncertainties in the single-seismic-parameter scaling relation can be comparable to, or smaller than, those from two parameter scaling relations.

First, we consider the case where we estimate radii, masses, and ages using seismic scaling relations in the same way as commonly done for *Kepler* and K2 ensemble analyses (e.g. Pinsonneault et al. 2018; Zinn et al. 2022). We use standard error propagation for mass uncertainties, and infer the age uncertainty based on the scaling relation from Bellinger (2020) (applicable only to red giant branch stars), for which we also needed a typical uncertainty in [Fe/H]. Typical TESS uncertainties are ∼ 5 per cent in ν_{max} and ∼ 3 per cent in $\Delta\nu$ (Fig. 7). From the Infrared Flux Method calibrated APOGEE survey, we can expect to be able to obtain T_{eff} with uncertainties in the range 40–80 K (Casagrande et al. 2010, 2021). We therefore adopt 80 K as a conservative random uncertainty value. This leads to typical random uncertainties of 8 per cent in radius, 19 per cent in mass, and 63 per cent in age [the latter assuming an uncertainty in [Fe/H] of 0.1 dex using the 'combination 1' formula of table 2 in Bellinger (2020)]. These uncertainties are dominated by the uncertainties in ν_{max} and $\Delta\nu$.

Systematic errors in T_{eff} are ∼2 per cent (Tayar et al. 2020). The 2 per cent pipeline-to-pipeline scatter in the seimic measurements would add a systematic of 4 per cent in radius, 8 per cent in mass, and 25 per cent in age. Likewise, the 2–3 per cent ν_{max} bias between TESS and *Kepler* at certain ν_{max} ranges (Fig. 8a) translates to a systematic of 2–3 per cent in radius, 6–9 per cent in mass, and 20–30 per cent in age.

Next, we consider the most common scenario where only ν_{max} is available. Because the seismic red giant sample from TESS is typically sampling the local neighbourhood (Hon et al. 2021), the stars have relatively small parallax uncertainties from *Gaia*. For our sample, the median *Gaia* radius uncertainties are ∼6 per cent (dominated by parallax uncertainty), assuming photometric temperature inferences and uncertainties, and hence our mass uncertainties are ∼12 per cent. This median mass uncertainty, dominated by the radius

uncertainty, roughly translates into an expected age uncertainty of 37 per cent on the red giant branch (Miglio 2012). In this scenario, the pipeline-to-pipeline systematics and the TESS-to-*Kepler* bias in $\nu_{\rm max}$ each translate to a systematic of only 2–3 per cent in mass and 6–9 per cent in age. *We therefore have the surprising, but robust, result that we can obtain ages with an interesting level of precision using $\nu_{\rm max}$ alone.*

Spectroscopic $T_{\rm eff}$ values will be available for large numbers of survey targets. They are of comparable precision to photometric $T_{\rm eff}$ values, but are not subject to systematic errors from extinction (and large metallicity) uncertainties. APOGEE, for example, is calibrated to be on the Infrared Flux Method scale, with well-controlled random and systematic errors. Spectra also give powerful composition information, important for inferring ages. The combination of spectroscopy, *Gaia*, and $\nu_{\rm max}$ is therefore likely to be the most fruitful technique for the full TESS asteroseismic sample.

Finally, we note that these estimates assume the 'typical' results (the median of the uncertainty distribution), and the error model is based on only 1–2 sectors of data. Clearly, the best fraction of stars will provide significant lower radius, mass, and age uncertainties. As an example, for the closest stars, parallax uncertainties are smaller, and hence the uncertainties in the bolometric corrections and $T_{\rm eff}$ (including the 2 per cent $T_{\rm eff}$ systematic error) will dominate the radius error budget. Considering only these stars, we would expect internal median radius uncertainties of 3–4 per cent, mass uncertainties of 8–9 per cent, and hence about 25–30 per cent in age, even when only $\nu_{\rm max}$ is measured. Also, the use of grid-based modelling (adding isochrone constraints on stellar inferences) will improve results, as demonstrated by Aguirre et al. (2020), who achieved ∼3 per cent in radius, ∼6 per cent in mass, and ∼20 per cent in age (internal uncertainties) when including *Gaia* parallaxes for stars with $\nu_{\rm max}$ and $\Delta\nu$ uncertainties similar to our sample. Uncertainties will, of course, also be lower for stars with longer time series (Hekker et al. 2012), which will be achieved with the ongoing extended TESS mission, especially in the continuous viewing zones (Mackereth et al. 2021). Photometry optimized for asteroseismology (Handberg et al. 2021; Lund et al. 2021) is also expected to lead to lower uncertainties and larger detection yields.

6 CONFUSION FROM BLENDS

TESS has relatively large pixels (21 arcsec on sky) compared to *Kepler* (3.98 arcsec), and blending is therefore expected to be more common with TESS. Blending can dilute the signal of target stars and hence lower detection yields (fig. 3; Mackereth et al. 2021). In addition, blends can cause 'confusion', where the seismic signal from one star is imposed on that of another. Among our red giant targets, we noticed this confusion when identifying the seismic detections. It manifested as two nearby stars showing almost identical power spectra, dominated by the star with the highest amplitude oscillations. In our case, confusion could only occur between red giants because less evolved stars oscillate at frequencies above the Nyquist frequency and with amplitudes too low to cause confusion (García & Stello 2015). To quantify how common confusion would typically be in a sample like ours, we applied a similarity measure on power spectra displayed in units of power density versus log frequency. The similarity that we used is known as the Shape-Based Distance (Paparrizos & Gravano 2015). It quantifies the correlation between two arrays, x and y, as $CC(x, y)/(\|x\|\|y\|)$, where CC is the cross-correlation operator and $\|\cdot\|$ indicates the vector norm. The Shape-Based Distance has a value of zero for a perfect correlation and −1 for a perfect anticorrelation. Before calculating the Shape-Based Distance between the TESS power spectra of two stars, we first bin each spectrum (in log units) into an array of length 1000. Next, we applied Gaussian smoothing with a kernel size of 15 to the binned spectrum and normalized the spectrum to have a mean value of zero and a standard deviation of one.

For each target star, we identified another star within our sample that has the smallest Shape-Based Distance. If this other star had an angular separation less than the typical photometric aperture to the target star (150 arcsec), it was flagged as a potential nearby blending star. To further vet blending star candidates, we ensured that the power was the same within the oscillation power excess for a target star and its candidate blending star. Using the binned and smoothed spectrum, we calculated the mean difference in power within the full width at half-maximum of the oscillation power excess ($\delta\nu_{\rm FWHM} = 0.59\nu_{\rm max}^{0.90}$; Mosser et al. 2010) between a target star and its blending companion. This power excess difference should be small for a correctly identified blending star compared to that of any other star that is not the true source of the blending. Therefore, each blending candidate was verified to be a blend only if its power excess difference puts it in the top 0.5 per cent percentile of most similar excesses compared to those of all other stars in our sample. This vetting process, combining Shape-Based Distance and power differences near $\nu_{\rm max}$, effectively identifies blends that have power spectra that are very similar to a target star.

A total of 85 targets, or about 1 per cent of our red giant sample, were found to be confused due to blending (counting any pair of

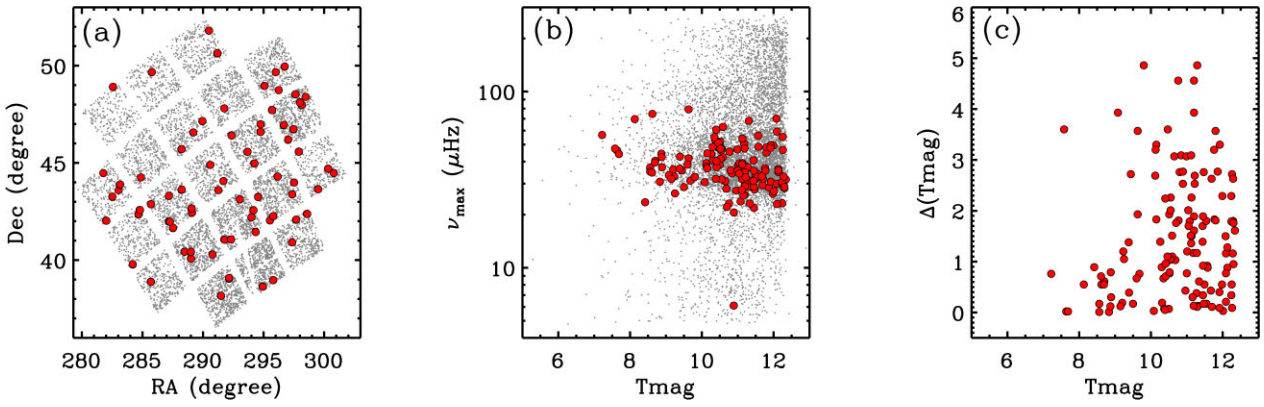

Figure 9. Location of blends (red dots) on the sky [panel (a)] and in the $\nu_{\rm max}$–$T_{\rm mag}$ plane [panel (b)]. Grey points are all stars in our sample as in Figs 1 and 3. Panel (c): Magnitude difference between target and blending star as a function of the target's magnitude.

blends only once). These stars did not show up as a particularly discrepant set in the previous figures. Fig. 9(a) shows the sky position of these blends, while Fig. 9(b) shows their location in the $\nu_{\rm max}$-$T_{\rm mag}$ plane. In Fig. 9(c), we show the difference in magnitudes between target and blending star as a function of the target's magnitude. So for seismic ensemble analyses of field red giants with TESS brighter than $T_{\rm mag}$ of 12.5, confusion due to blending is a relatively minor issue. Towards fainter magnitudes (and in particularly crowded fields), the issue will of course be more severe. However, Fig. 3 shows that we can only expect to detect oscillations in fainter stars if they are quite luminous, which comprises a small fraction of all red giants that TESS will be able to detect oscillations in.

7 CONCLUSION

Our findings, based on 1–2 sectors of TESS data, can be summarized as the following:

(i) Due to photon noise, oscillations are typically not detectable in low luminosity red giant stars ($\nu_{\rm max} \gtrsim 150$ μHz; $\log g \gtrsim 3.1$ dex) except for the brightest stars ($T_{\rm mag} \lesssim 8 - 9$). This is in agreement with Mosser et al. (2019, their fig. 10).

(ii) Our results suggest TESS will be able to detect oscillations down to $T_{\rm mag} \sim 14$ for the most luminous giants ($\nu_{\rm max} \lesssim 10$ μHz; $\log g \lesssim 1.9$).

(iii) Of the stars with detected oscillations we can measure $\Delta\nu$ reliably in about 20 per cent of them, but this yield depends a lot on the type of star (its $\nu_{\rm max}$ and if it is He-core burning or not) and the amount of TESS data available.

(iv) We find the median random uncertainty is 5–6 per cent for $\nu_{\rm max}$ and 2–3 per cent for $\Delta\nu$, which for common grid-modelling approaches should yield uncertainties of 3 per cent in radius, 6 per cent in mass, and 20 per cent in age (Aguirre et al. 2020).

(v) For stars with only a $\nu_{\rm max}$ measurement – the most common case for TESS – we obtain median uncertainties of 6 per cent in radius and 12 per cent in mass (hence expected 37 per cent in age) based on the $\nu_{\rm max}$ scaling relation and *Gaia* parallax measurements.

(vi) Systematics in the $T_{\rm eff}$ scale, pipeline-to-pipeline scatter in the seismic results, and bias between TESS and *Kepler* results each translate to systematics of 2–3 per cent in radius, 6–9 per cent in mass, and 20–30 per cent in age.

(vii) Our blending analysis of the *Kepler* field, which sits between Galactic latitudes of 6 and 21 °, suggests confusion of seismic signals from neighbouring stars due to blending is not expected to affect more than 1 per cent of red giants observed by TESS.

Finally, we note that this investigation is based on a single set of light curves. It would be desirable in future to quantify detection yields from independent asteroseismic-optimised light curves when they become available in the *Kepler* field, such as the forthcoming TASOC light curves (Handberg et al. (2021); Lund et al. (2021).

ACKNOWLEDGEMENTS

We thank Kosmas Gazeas for comments on the manuscript. D.S. is supported by the Australian Research Council (DP190100666). N.S. and D.H. acknowledge support from the National Aeronautics and Space Administration (80NSSC18K1585, 80NSSC20K0593) awarded through the TESS Guest Investigator Programme. D.H. also acknowledges support from the Alfred P. Sloan Foundation. T.R.B. is supported by the Australian Research Council (DP210103119). R.A.G. acknowledges the support from the PLATO CNES grant. S.M. acknowledges support by the Spanish Ministry of Science and Innovation with the Ramon y Cajal fellowship number RYC-2015-17697 and the grant number PID2019-107187GB-I00.

DATA AVAILABILITY

The data underlying this article are available on request.

REFERENCES

Aguirre V. S. et al., 2020, ApJ, 889, L34
Anders F. et al., 2017, A&A, 597, A30
Bedding T. R. et al., 2010, ApJ, 713, L176
Bellinger E. P., 2020, MNRAS, 492, L50
Brasseur C. E., Phillip C., Hargis J., Mullally S., Fleming S., Fox M., Smith A., 2019, in Teuben P. J., Pound M. W., Thomas B. A., Warner E. M., eds, ASP Conf. Ser. Vol. 523, Astronomical Data Analysis Software and Systems XXVII. p. 397
Brown T. M., Gilliland R. L., Noyes R. W., Ramsey L. W., 1991, ApJ, 368, 599
Campante T. L. et al., 2016, ApJ, 830, 138
Casagrande L., Ramírez I., Meléndez J., Bessell M., Asplund M., 2010, A&A, 512, A54
Casagrande L. et al., 2016, MNRAS, 455, 987
Casagrande L. et al., 2021, MNRAS, 507, 2684
Chaplin W. J. et al., 2011, Science, 332, 213
de Ridder J. et al., 2009, Nature, 459, 398
Elsworth Y., Hekker S., Basu S., Davies G. R., 2017, MNRAS, 466, 3344
Gaia Collaboration et al., 2018, A&A, 616, A1
García R. A., Stello D., 2015, Extraterrestrial Seismology. Cambridge Univ. Press, Cambridge, p. 159
García R. A. et al., 2014, A&A, 568, A10
Handberg R. et al., 2021, AJ, 162, 170
Hekker S. et al., 2010, MNRAS, 402, 2049
Hekker S. et al., 2011, MNRAS, 414, 2594
Hekker S. et al., 2012, A&A, 544, A90
Hon M., Stello D., Yu J., 2018a, MNRAS, 476, 3233
Hon M., Stello D., Zinn J. C., 2018b, ApJ, 859, 64
Hon M., Stello D., García R. A., Mathur S., Sharma S., Colman I. L., Bugnet L., 2019, MNRAS, 485, 5616
Hon M. et al., 2021, ApJ, 919, 131
Howell S. B. et al., 2014, PASP, 126, 398
Huber D., Stello D., Bedding T. R., Chaplin W. J., Arentoft T., Quirion P., Kjeldsen H., 2009, Commun. Asteroseismology, 160, 74
Huber D. et al., 2011, ApJ, 743, 143
Kallinger T. et al., 2010a, A&A, 509, 77
Kallinger T. et al., 2010b, A&A, 522, 1
Khan S. et al., 2019, A&A, 628, A35
Kjeldsen H., Bedding T. R., 1995, A&A, 293, 87
Lightkurve Collaboration et al., 2018, Astrophysics Source Code Library, record ascl:1812.013
Lund M. N. et al., 2021, ApJS, 257, 53
Mackereth J. T. et al., 2021, MNRAS, 502, 1947
Mathur S. et al., 2010, A&A, 511, A46
Miglio A., 2012,in Montalban J., Noels A.,eds, Astrophys. Space Sci. Proc. Vol. 26, Red Giants as Probes of the Structure and Evolution of the Milky Way, Springer-Verlag, Berlin, p. 11
Miglio A. et al., 2009, A&A, 503, L21
Miglio A. et al., 2013, MNRAS, 429, 423
Mosser B., Appourchaux T., 2009, A&A, 508, 877
Mosser B. et al., 2010, A&A, 517, 22
Mosser B. et al., 2012, A&A, 537, A30
Mosser B., Michel E., Samadi R., Miglio A., Davies G. R., Girardi L., Goupil M. J., 2019, A&A, 622, A76

Paparrizos J., Gravano L., 2015, in Proceedings of the 2015 ACM SIGMOD International Conference on Management of Data - SIGMOD, k-shape: Efficient and Accurate Clustering of Time Series. ACM Press, New York
Pinsonneault M. H. et al., 2014, ApJS, 215, 19
Pinsonneault M. H. et al., 2018, ApJS, 239, 32
Rendle B. M. et al., 2019, MNRAS, 490, 4465
Reyes C., Stello D., Hon M., Zinn J. C., 2022, MNRAS, 511, 5578
Ricker G. R. et al., 2015, J. Astron. Telesc. Instrum. Syst., 1, 014003
Saunders N. et al., 2021, AJ, 163, 53
Schofield M. et al., 2019, ApJS, 241, 12
Sharma S., Stello D., Bland-Hawthorn J., Huber D., Bedding T. R., 2016, ApJ, 822, 15
Sharma S. et al., 2019, MNRAS, 490, 5335
Sharma S., Stello D., Zinn J. C., Bland-Hawthorn J., 2021a, preprint (arXiv:2109.12173)
Sharma S. et al., 2021b, MNRAS, 506, 1761
Silva Aguirre V. et al., 2018, MNRAS, 475, 5487
Stassun K. G. et al., 2019, AJ, 158, 138
Stello D., Bruntt H., Preston H., Buzasi D., 2008, ApJ, 674, L53
Stello D. et al., 2015, ApJ, 809, L3
Stello D. et al., 2017, ApJ, 835, 83
Tayar J., Claytor Z. R., Huber D., van Saders J., 2020, preprint (arXiv:2012.07957)
Yu J., Huber D., Bedding T. R., Stello D., Hon M., Murphy S. J., Khanna S., 2018, ApJS, 236, 42
Zinn J. C., Stello D., Huber D., Sharma S., 2019, ApJ, 884, 107
Zinn J. C. et al., 2020, ApJS, 251, 23
Zinn J. C. et al., 2022, ApJ, 926, 191

This paper has been typeset from a TEX/LATEX file prepared by the author.